

Information-Guided Dynamic Nuclear Polarization


Santiago Bussandri^{1,2}, Gerónimo Sequeiros^{1,2}, Pablo R. Zangara^{1,2}, Rodolfo H. Acosta^{1,2} and Carlos A. Meriles^{3,4,*}

¹*Facultad de Matemática, Astronomía, Física y Computación, Universidad Nacional de Córdoba, Córdoba, Argentina*

²*CONICET, Instituto de Física Enrique Gaviola (IFEG), Córdoba, Argentina*

³*Department of Physics, CUNY-City College of New York, New York, New York 10031, USA*

⁴*CUNY-Graduate Center, New York, New York 10016, USA*

 (Received 26 January 2022; revised 2 May 2022; accepted 9 August 2022; published 15 September 2022)

A spin ensemble in thermal equilibrium continuously undergoes random fluctuations analogous to those observed in Brownian motion, a process known as spin noise. Here, we investigate the dynamics of a system comprising a spin-1 paramagnetic center and a hyperfine-coupled spin-1/2 nucleus in the vicinity of a level crossing. We theoretically show that nuclear spins polarize efficiently under the combined action of thermal fluctuations and a closed-loop feedback protocol. The latter articulates periodic observations of the electronic magnetization and radio-frequency pulses connecting hybrid states with opposite nuclear spin alignment. Since nuclear polarization emerges from electronic spin fluctuations, not spin order, this microwave-free technique generically benefits from warmer, not colder, operation temperatures. Furthermore, because the spin dynamics at play near a level crossing is rather insensitive to the absolute value of the magnetic field, our work promises opportunities for high-field dynamic nuclear polarization, which is difficult to attain through present methods.

DOI: [10.1103/PhysRevApplied.18.034039](https://doi.org/10.1103/PhysRevApplied.18.034039)

I. INTRODUCTION

Starting with Maxwell's thought experiment of a "demon" controlling the particle flow between two separate baths [1], the notion of creating order from disorder has, ever since, captured the imagination of scientists. First thought to violate the second law of thermodynamics, the idea that one can leverage thermal fluctuations presently attracts widespread attention, as it underlies fundamental discussions on the operation of microscopic heat engines [2] or the generation of one-directional propagation out of Brownian motion [3,4]. Along related lines, the use of informational feedback in noisy systems—a concept also central to the present work—is garnering significant interest because of its broad relevance in subjects ranging from population dynamics [5] to economics [6] and biochemical signaling networks [7].

Spin ensembles are not immune to fluctuations, hence providing a natural platform to extend the above ideas. Indeed, soon after the introduction of nuclear magnetic resonance, Bloch [8] hypothesized that an ensemble containing N spins in thermal equilibrium would induce voltage fluctuations in a magnetic sensor proportional to \sqrt{N} , an insight subsequently confirmed via inductive [9] and

superconducting quantum interference device (SQUID) [10] measurements. Building on these fundamental observations, "spin noise" is exploited, e.g., to obtain spectroscopic information from nuclear [11] and atomic vapor [12] spin ensembles or to reconstruct images [13] without the need for radio-frequency excitation. Spin noise also lies at the heart of nanoscale magnetometry techniques based on the properties of nitrogen-vacancy centers in diamond [14,15]. Furthermore, magnetic resonance force microscopy allows the implementation of real-time-feedback techniques to rectify thermal spin fluctuations and ultimately spin polarize a microscopic ensemble of paramagnetic centers [16,17] or nuclear spins [18]. These latter studies align with broad ongoing work on dynamic nuclear polarization (DNP), presently attracting intense interest as a route to enhance the sensitivity of nuclear magnetic resonance [19,20].

Here, we consider a spin set formed by a paramagnetic center with spin number $S = 1$ and a neighboring nuclear spin $I = 1/2$. We assume spin S features a crystal field of amplitude, Δ , and tune the externally applied magnetic field, B , somewhere near the level-crossing condition, $|\gamma_e|B_c = \Delta$, where γ_e denotes the electronic spin gyromagnetic ratio. By implementing a closed-loop feedback protocol based on real-time monitoring of the electronic magnetization—fluctuating around

*cmeriles@ccny.cuny.edu

the thermal equilibrium value—we theoretically show that hyperfine-coupled nuclear spins can be dynamically polarized through the use of radio-frequency (rf) pulses, the frequency of which is actively adjusted to address different pairs of states with opposite nuclear- (and electronic) spin orientations. This form of “informational” dynamic nuclear polarization (IDNP) does not rely on electronic spin polarization, and hence, does not necessarily depend on cryogenic temperatures and/or high magnetic fields (provided the detector sensitivity remains high); furthermore, operation near the level crossing makes the use of microwave unnecessary.

II. RESULTS

To lay out our technique, we first introduce the Hamiltonian for the two-spin system,

$$H = \Delta S_z^2 - \gamma_e B S_z - \gamma_n B I_z + A_{zz} S_z I_z + A_{zx} S_z I_x, \quad (1)$$

where γ_e and γ_n , respectively, represent the electron and nuclear gyromagnetic ratios; Δ denotes the crystal-field amplitude on spin S , and B is the applied magnetic field, here assumed to be parallel to the crystal-field axis. The secularized hyperfine interaction [21] is defined by the coupling parameters A_{zz} and A_{zx} . Equation (1) is quite general, in the sense that it applies to a broad family of electronic-nuclear spin pairs, even if, for illustration purposes, we might choose particular spin species (see below).

We first consider the two-dimensional diagram in Fig. 1(a) where we group the eigenstates $|m_S, m_I\rangle$ of the two-spin set according to their energy, E , and electronic magnetization, M_e (vertical and horizontal axes in the diagram, respectively). Throughout our calculations, we set

the field amplitude, B , close to—though slightly shifted from—the level-crossing field, B_c , defined as $|\gamma_e|B_c = \Delta$. While the exact energy detuning, $\delta_e = |\gamma_e|(B - B_c)$ —or, equivalently, δ_n , see Fig. 1(a)—is not uniquely defined, the energy mismatch is assumed to be sufficiently large so as to preempt cross relaxation [22–24]. Furthermore, we assume the chosen value—inconsequential in the polarization protocols we introduce below—ensures our ability to invert the populations of states $|0, -1/2\rangle$ and $|-1, +1/2\rangle$ [or $|0, +1/2\rangle$ and $|-1, -1/2\rangle$, see Fig. 1(a) for notation] with pulses at frequencies ω_α (or ω_β) in the rf range. Reproducing the standard configuration in DNP, we also assume the above two-spin set is part of a molecule, the “polarizing agent,” several copies of which are uniformly distributed throughout the host crystal [Fig. 1(b)]. Each of these units serves as the source of spin order for surrounding nuclei, polarizing via spin-diffusion processes driven by internuclear couplings or mediated through electron-spin interactions [25–27].

While the mean occupation probabilities of a spin system in thermal equilibrium are dictated by the Boltzmann distribution, the populations of all levels undergo thermal fluctuations, the mean amplitude of which grows with the number of particles N_e in the ensemble as $\sqrt{N_e}$. The time dynamics of these fluctuations are governed by the electronic spin–lattice-relaxation time, T_{1e} , which can be used to calculate the interstate transition rates in thermal equilibrium, and hence, model the system’s time evolution throughout a given Monte Carlo realization (see Appendix A). One example is shown in Fig. 2(a), where we display the time trace of ΔM_e , the change of electronic magnetization relative to its thermal value, for an ensemble of 10^6 (independent) polarizing agents.

An interesting characteristic in the spin system in Fig. 1 is that, even though populations in the nearly degenerate

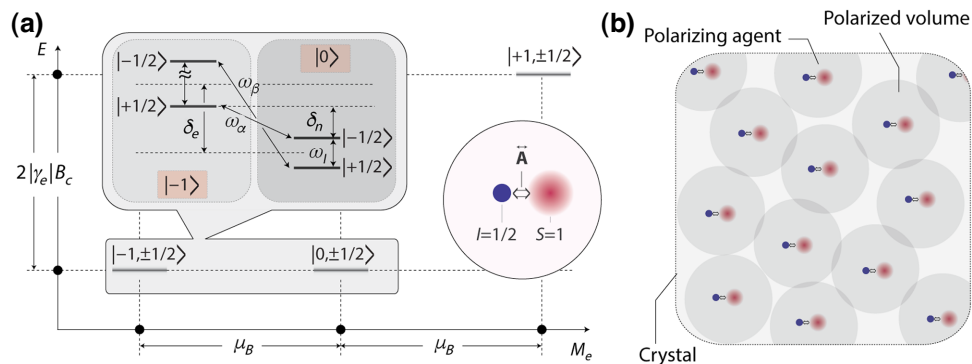


FIG. 1. Spin model. (a) Circled inset, we consider a spin set comprising an electronic spin $S = 1$ coupled to a nuclear spin $I = 1/2$ via the hyperfine tensor \vec{A} . Main, system eigenstates organized by energy, E , and magnetization, M_e (vertical and horizontal axes, respectively), assuming a magnetic field close to B_c . Square inset, magnified view of the energy-level structure corresponding to the enclosed states; we assume a small detuning, δ_e , away from the level anticrossing. (b) In our simulations, we consider an ensemble of two-spin molecules (the polarizing agent) imbedded in a solid-state matrix; each one serves as the polarization source for a range of surrounding nuclei (dark circles).

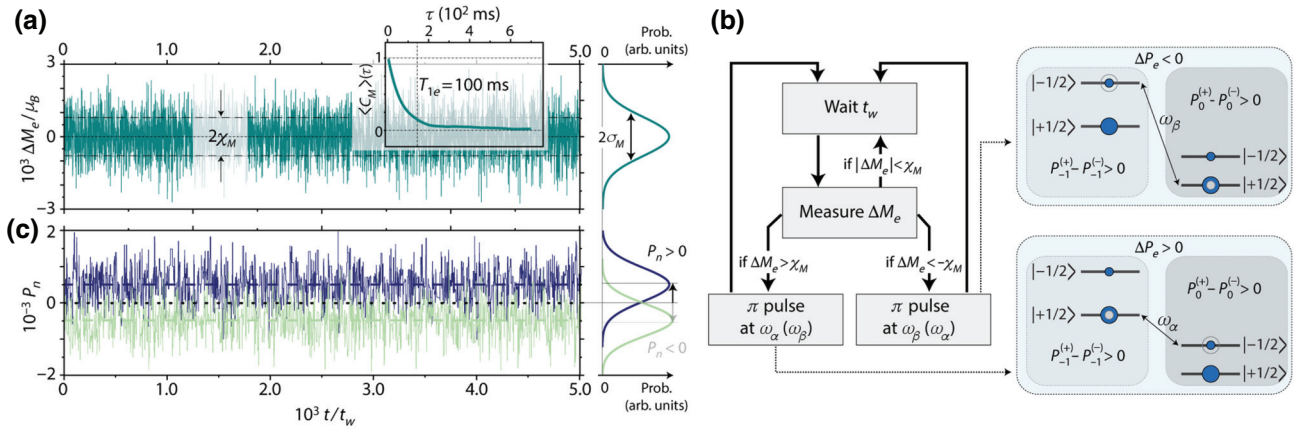


FIG. 2. Extracting nuclear polarization from electronic spin noise. (a) Time trace of the electronic magnetization change, ΔM_e , relative to the equilibrium value at $T = 80$ K in an ensemble of $N = 10^6$ independent spin sets; electronic spin-lattice-relaxation time is $T_{1e} = 100$ ms. Upper and lower dashed lines indicate rf-pulse activation thresholds. Inset is the spin-noise correlation function, as extracted from the time trace of ΔM_e . (b) Dynamic-nuclear-polarization protocol configured to produce positive nuclear polarization. Changing the rf frequencies to the values in parentheses reverses the sign of the resulting polarization. (c) Blue, time trace of nuclear polarization upon repeated application of the protocol in (b). Faint green, same as above, but for the case where the frequencies in the inversion pulses are reversed. Central dashed line indicates the thermal value. Throughout these simulations, we assume $\Delta = 28.05$ GHz, $B = 1$ T, $|\delta_e| = 20.7$ MHz, $|\delta_n| = 5$ MHz, and $A_{zz} = A_{zx} = 10$ MHz; pulse-triggering threshold is $\chi_M = \sigma_M$ and the wait time between pulses is $t_w = T_{1e}$. In (a),(c), the histograms on the right represent normalized distributions derived from the corresponding time traces.

states $|m_S = 0\rangle$ and $|m_S = -1\rangle$ are (on average) virtually the same, the magnetic moments associated with each of them, 0 and $-\mu_B$, respectively, are markedly different [see horizontal axis in Fig. 1(a)]. Therefore, a change in magnetization towards values lower than those in equilibrium (i.e., $\Delta M_e < 0$) signals (probabilistically) a transient growth in the integrated population $P_{-1} \equiv P_{-1}^{(+)} + P_{-1}^{(-)}$ of the $|m_S = -1\rangle$ manifold (superscripts allude to the nuclear quantum number, m_I); conversely, the observation of $\Delta M_e > 0$ preferentially indicates a temporary increase in the system's population, $P_0 \equiv P_0^{(+)} + P_0^{(-)}$, within $|m_S = 0\rangle$.

Building on the monitoring of ΔM_e , the key to creating nuclear-spin order resides in the ability to selectively invert the populations of states $|0, -1/2\rangle$ and $|-1, +1/2\rangle$ (or $|0, +1/2\rangle$ and $|-1, -1/2\rangle$) contingent on the observed value of magnetization. Net nuclear polarization, $P_n = \sum_{i=-1}^1 (P_i^+ - P_i^-)$, emerges upon rf excitation because, for a nonzero population difference $\Delta P_e \equiv P_0 - P_{-1}$, a π pulse at frequency ω_α (or ω_β) leads to a nuclear-spin imbalance proportional to ΔP_e [see Fig. 2(b)]. Importantly, the sign of the imbalance changes depending on the pair of states targeted by the rf pulse; therefore, nuclear-spin polarization can be created and maintained over time if the experimenter adjusts the pulse frequency every time the sign of ΔP_e changes. Furthermore, as a quick inspection of the diagram in Fig. 2(b) shows, the sign of the resulting nuclear polarization reverses if one alters the pairing between rf frequencies and electronic spin

fluctuations. This is shown in the upper (lower) time traces of Fig. 2(c), where we generate and maintain positive (negative) nuclear polarization by tuning the rf pulse to ω_α for $\Delta P_e > 0$ and ω_β for $\Delta P_e < 0$ (respectively, ω_α for $\Delta P_e < 0$ and ω_β for $\Delta P_e > 0$).

Although ΔM_e takes random values from a Gaussian distribution of width σ_M [see histogram on the right-hand side of Fig. 2(a)], changes in the system's magnetization do not occur arbitrarily fast, since the electronic spin-lattice-relaxation time, T_{1e} , is finite. The latter translates into a non-null time-correlation function, $C_M(\tau) = \langle \Delta M_e(t + \tau), \Delta M_e(t) \rangle / \sigma_M^2 \approx \exp(-\tau/\tau_1)$, the characteristic time constant of which satisfies $\tau_1 \sim T_{1e}$. Correspondingly, we conclude that the end nuclear-spin polarization remains unchanged if we adjust the wait time, t_w , between successive rf pulses so that $t_w \gtrsim T_{1e}$ (we are assuming the timescale governing nuclear-spin lattice relaxation is sufficiently long so as to be ignored).

The above results assume instantaneous inversion pulses, an idealized limit that is justified as long as the finite rf duration is much shorter than the characteristic time of the dynamics at play (in this case, governed by T_{1e}). This condition is not difficult to attain for strongly coupled electron-nuclear-spin pairs because the pseudosecular contribution to the Hamiltonian [last term in Eq. (1)] hybridizes the $|\pm 1/2\rangle$ nuclear-spin states, hence enabling otherwise forbidden transitions at ω_α and ω_β (Appendix B). For example, for hyperfine couplings on the order of 10 MHz and a magnetic field $B \sim B_c \sim 1$ T, we find Rabi frequencies of $\Omega_{rf} \gtrsim 1$ MHz (or inversion

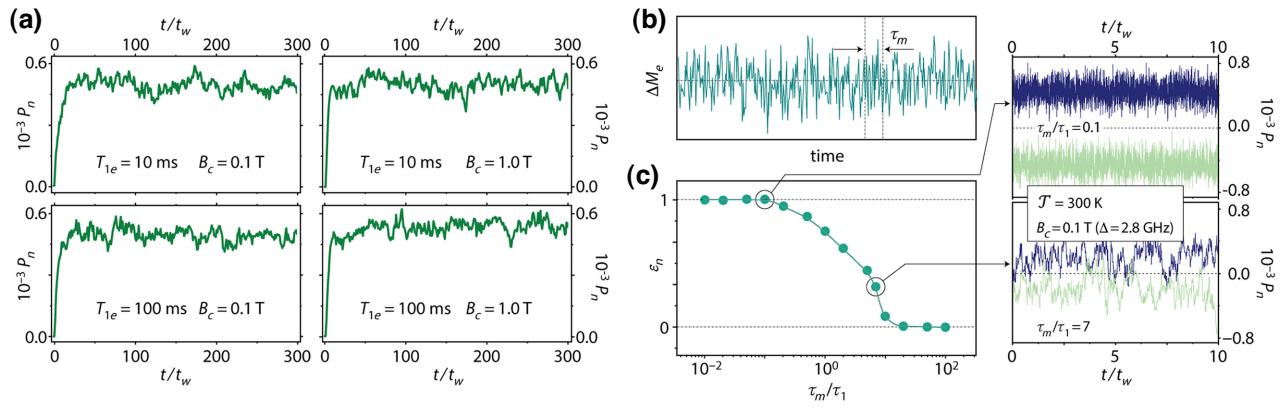


FIG. 3. Impact of electron spin–lattice-relaxation time. (a) Calculated nuclear polarization as a function of time using the protocol of Fig. 2(b) for different spin-lattice times, T_{1e} , and level-crossing fields, B_c ; we set the temperature at $T = 300$ K. To reduce dispersion, we average over 200 runs of the same protocol. (b) Schematic of magnetization change as a function of time. Realistic observation demands a finite measurement time, τ_m . (c) Nuclear-spin polarization efficiency as a function of the fractional measurement time, τ_m/τ_1 . Insets on the right-hand side of the plot illustrate two limit cases. Unless indicated, all conditions are the same as those in Fig. 2.

pulses in the few-hundred-nanosecond range), assuming only moderate rf fields. Note that the above conditions do not differ from those typical in standard DNP applications [19], except that, in the present case, operation near B_c allows us to bring down the excitation frequency from the microwave to the rf range.

Since the polarization process depends only on the amplitude of the electronic spin fluctuations, the steady-state value for P_n must be largely insensitive (at least from a conceptual point of view) to the exact value of T_{1e} and operating magnetic field, $B \sim B_c$, or temperature (see below). Figure 3(a) contains a numerical demonstration where we consider alternative scenarios. Remarkably, we find the same end nuclear-spin polarization in all cases (even though T_{1e} does impact the polarization growth rate at early times). We warn, however, that the

absolute values of nuclear polarization we derive here must be interpreted as the upper limit because our numerical modeling does not take into account spin-lattice relaxation of bulk nuclei, which, in general, will have a negative impact (see Appendix A). For completeness, we mention that the above polarization strategy fails if the paramagnetic center also has a spin number equal to $1/2$ because the two transition frequencies associated with pairs of states with opposite electronic and nuclear-spin orientation—featuring frequencies $(|\gamma_e| \pm \gamma_n)B$ —become nearly identical if, as assumed, the electronic Zeeman frequency is in the rf range.

Naturally, every realistic measurement device has a finite sensitivity, meaning that a minimum measurement time, τ_m , is required to determine the system’s magnetization [Fig. 3(b)]. As τ_m becomes comparable to τ_1 , the lag in

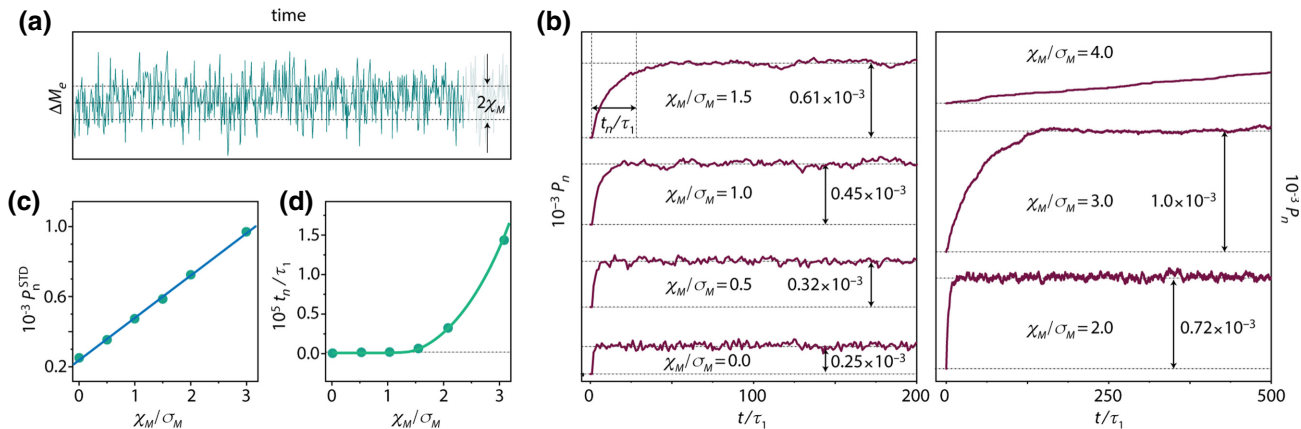


FIG. 4. Attaining optimal end polarization. (a) Schematic of magnetization fluctuation as a function of time; we investigate the impact of the pulse-activation threshold, χ_M , on the steady-state nuclear polarization, P_n^{STD} . (b) Time trace of the nuclear polarization for different pulse-activation thresholds χ_M . (c) Steady-state nuclear polarization as a function of the relative pulse-activation threshold χ_M/σ_M . (d) Characteristic build-up time fraction, t_n/τ_1 , as a function of χ_M/σ_M . In (c),(d), solid lines are guides to the eye.

the information flow has an increasingly negative impact on the polarization process because the inversion pulses become ineffective if the system has randomly changed its configuration at the time they are applied. This is shown in Fig. 3(c), where we plot the calculated steady-state polarization efficiency, $\varepsilon_n \equiv P_n^{\text{STD}}/P_n^{\text{opt}}$ —defined as the fractional steady-state polarization relative to the optimum obtained in the limit $\tau_m \rightarrow 0$ —as a function of the fractional measurement time τ_m/τ_1 . As shown on the right-hand side inset of Fig. 3(c), we attain a substantially reduced polarization when $\tau_m/\tau_1 \sim 7$. Provided τ_m is sufficiently short, however, the steady-state polarization is identical to that observed in Fig. 2, despite the unfavorable magnetic field and temperature (0.1 T and 300 K, respectively).

While correlating the pulse frequency with the sign of ΔM_e always leads to net nuclear-spin polarization, the steady-state amplitude depends on the chosen pulse-activation threshold, χ_M [Fig. 4(a)]. Figure 4(b) shows some examples where we express χ_M as a fraction of σ_M , the root mean square of $\Delta M_e(t)$, for a variable fractional time t/τ_1 . Greater pulse-activation thresholds monotonically lead to greater end nuclear polarization [Fig. 4(c)]; unfortunately, the characteristic (fractional) build-up time, t_n/τ_1 , quickly diverges as enabling events become too rare, thus imposing a practical limit [Fig. 4(d)].

A somewhat similar interplay is shown in Fig. 5 where we calculate the end nuclear-spin polarization as a function of the number, N_e , of electronic spins in the ensemble. Even though the *absolute* amplitude of the magnetization fluctuations grows as $\sqrt{N_e}$, the average polarization transferred per unit electronic spin scales with the *relative* amplitude of the magnetization fluctuation, thus leading to a $1/\sqrt{N_e}$ dependence [Fig. 5(a)]. Taking the room-temperature ^{13}C polarization at 10 T as a crude reference (in the order of 10^{-5}), we conclude that meaningful polarization levels can be attained in systems containing up to about 10^9 electronic spins. In a system where every electronic spin polarizes 10^6 surrounding nuclear spins—equivalent to about 1-ppm concentration of polarizing agents—the latter crudely amounts to a $30\text{-}\mu\text{m}^3$ crystal.

Interestingly, the above estimates implicitly assume independence between the statistics governing spin-lattice relaxation in physically separate electronic spins. This is, of course, no longer true, e.g., if the polarizing agent concentration is sufficiently high (so that the interaction between electronic spins in different polarizing agents is non-negligible) or if the presence of a high- Q cavity creates effective interspin couplings. While a quantum mechanical calculation that takes these interactions into account is in general too complex, one can qualitatively describe the many-body dynamics at play through an *ad hoc* correlation (or anticorrelation) between electron-spin–lattice-relaxation events at different sites.

Using $C_+ \in [0, 1]$ ($C_- \in [0, 1]$) to parametrize alignment (antialignment), Fig. 5(b) presents an illustration where relaxation probabilities are adjusted so that immediate neighbors tend to be parallel ($C_+ = 0.5$) or antiparallel ($C_- = 0.5$) at all times. Since correlations (anticorrelations) tend to amplify (reduce) the average amplitude of $\Delta M_e(t)$ —and, correspondingly, $\Delta P_e(t)$ —we observe a growth (decrease) in the average nuclear polarization, P_n [Fig. 5(b)].

III. CONCLUSION

We introduce an alternative path to dynamic nuclear polarization that builds on the thermal fluctuations of the electronic spin magnetization away from the equilibrium value at a given temperature. Unlike traditional methods, the present strategy leverages the information accrued in real time about the “instantaneous” amplitude of the electronic magnetization. The energy structure produced near a level anticrossing allows for the use of selective radio-frequency pulses, which are comparatively simpler to produce than high-power microwave. As presented, the bandwidth is simply dictated by the inverse pulse duration, though broader excitation can be attained through the use of composite pulses or partial field sweeps [28] that recreate the dynamics of the “integrated solid effect” [29]. The implementation of these or related protocols, however, is contingent on their duration, which must remain shorter than T_{1e} .

Ideally, the end nuclear polarization is solely dictated by the relative amplitude of the electronic magnetization fluctuations, which render the protocol insensitive to the operating magnetic field and temperature. Furthermore, assuming the concentration of the polarizing agent is fixed, P_n is greater for smaller samples, which favors application to the investigation of mass-limited systems. Identifying the optimal working conditions is complex, however, due to the interplay between the finite sensitivity of a realistic detector and the temperature and field dependence of the electronic spin–lattice-relaxation time.

Interestingly, electronic or nuclear-state hybridization near a level crossing is expected to preserve the polarization efficiency of rf excitation, even at high fields [30]. This feature compares favorably with regular DNP, where polarization mechanisms, such as the solid effect, become less effective as the field grows due to gradual truncation of the pseudosecular term [31]. Level crossing at high fields can be attained, e.g., through the use of molecules hosting a rare-earth ion, where zero-field splittings of up to about 10 THz are possible [32].

While an in-depth discussion of the experimental implementation falls beyond the scope of this article, there are several magnetic sensing techniques whose high detection sensitivity could be exploited for this application

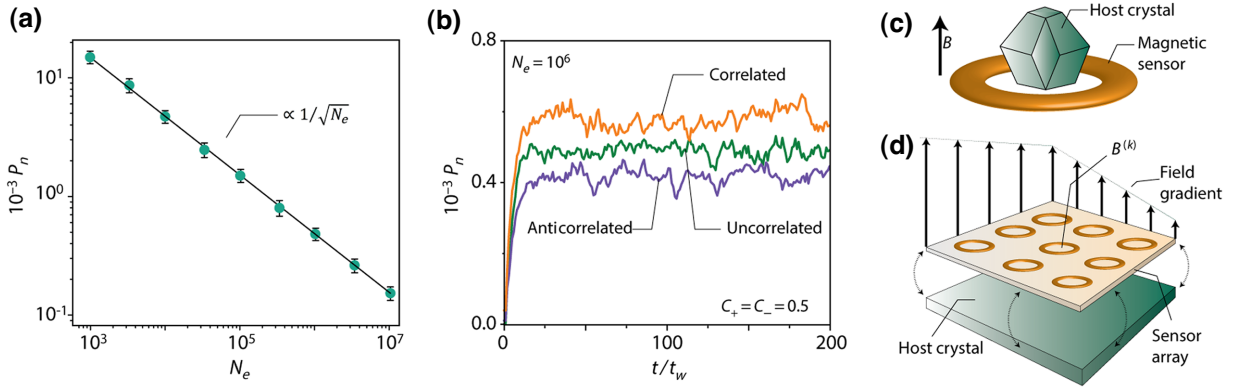


FIG. 5. Interplay between number of electronic spins and nuclear polarization. (a) Average nuclear-spin polarization as a function of N_e , assuming the conditions in Fig. 2. (b) Time traces of nuclear polarization for an ensemble of 10^6 polarizing agents in a chain with an underlying partial correlation ($C_+ = 0.5$) or anticorrelation ($C_- = 0.5$) between the spin alignment of immediate electronic spin neighbors; for reference, we also include the uncorrelated case (where $C_{\pm} = 0$). Correlations (anticorrelations) increase (decrease) the mean square amplitude of the electronic fluctuations (not shown), and thus, change the end polarization compared to the case where all spin sets evolve independently. Throughout these simulations, we assume $B_c = 1$ T; all other conditions are the same as those in Fig. 2. (c) Schematics of a detection setup. To attain the highest nuclear polarization, the sample size must be kept small. (d) To polarize a bulk sample, one could resort to an array of magnetic sensors, each informing on the local electronic spin polarization; a magnetic field gradient defines a local magnetic field $B^{(k)}$ at site k , hence allowing for selective rf manipulation at each sensor site.

[Fig. 5(c)]. One possibility is the use of giant magnetoresistive sensors, broadly deployed for *in vitro* biological detection of proteins attached to magnetic tags, and other biomedical applications at room temperature [33,34]. An alternative platform is chip-integrated SQUID technology [35,36], recently proven to operate over a wide range of magnetic fields exceeding 1.5 T and with sensitivities of up to $0.38 \mu_B/\sqrt{\text{Hz}}$.

An intriguing question open to further investigation is whether IDNP could be applied to macroscopic samples, perhaps through the use of a sensor array covering a larger target area [Fig. 5(d)]. In such a system, parallelized information retrieval on local electronic magnetization could be converted into massive nuclear magnetization through a field gradient designed to render the action of the rf pulses site selective. It is presently unclear, however, whether technical complications, such as detector crosstalk—necessarily dependent on the chosen sensing device—can be overcome.

ACKNOWLEDGMENTS

Work by C.A.M. is supported by the U.S. Department of Energy (DOE), Office of Science, Basic Energy Sciences (BES), under Award No. BES-DE-SC0020638; he also acknowledges access to the facilities and research infrastructure of the NSF CREST IDEALS, Grant No. NSF-HRD-1547830. S.B., G.S., P.R.Z., and R.H.A. acknowledge financial support from SeCyT-UNC (Grant No. 33620180100154 CB) and CONICET (Grant No. PIP 11220200102451CO).

APPENDIX A: MONTE CARLO MODELING

In this section, we provide details on the numerical approach we use in our calculations. Given the two-spin Hamiltonian introduced in Eq. (1), we calculate the equilibrium density matrix for a given temperature as

$$\rho_0 = \frac{\exp(-H/k_B T)}{\text{Tr}\{\exp(-H/k_B T)\}}. \quad (\text{A1})$$

The state of the ensemble of polarizing agents (two-spin systems) is obtained by means of a Monte Carlo direct sampling of ρ_0 . Each polarizing agent is then initialized in a state with a probability given by the diagonal matrix elements of ρ_0 . The average population of each ensemble state, i.e., $P_{m_S}^m$, can be computed by adding the contribution of each polarizing agent. These populations are then used to calculate the electronic population difference, $\Delta P_e = P_0 - P_{-1}$; nuclear population, $P_n = \sum_{i=-1}^1 (P_i^+ - P_i^-)$; and the corresponding magnetizations.

We introduce time-dependent dynamics in the model by allowing each agent to change its state according to the transition rates:

$$W_{i,j} = \frac{1}{T_{1e}(1 + e^{(E_j - E_i)/k_B T})}. \quad (\text{A2})$$

Here, E_j (E_i) is the energy of state j (i), and T_{1e} is the electronic longitudinal relaxation time. These rates are transformed into transition probabilities per unit time, which are then used to evolve each Monte Carlo realization.

To define the pulse-triggering threshold, χ_M , we sample ρ_0 , let the ensemble evolve, and monitor the fluctuations

of the electronic magnetization around its mean value, see Fig. 2(a). The pulse threshold, χ_M , is then chosen to be proportional to the width of such fluctuations, as quantified by σ_M .

As shown in Figs. 3 and 4, nuclear polarization build-ups follow from the generic procedure sketched in Fig. 2(b). In addition to intrinsic dynamics induced by the internal rates, $W_{i,j}$, the external driving is simulated by instantaneous π pulses inducing population swaps between two targeted states. This approach is justified, as long as the pulse duration is much shorter than T_{1e} , a condition that can be attained with only moderate rf field amplitudes (Appendix B).

We stress our approach accounts only for the average nuclear polarization at the polarizing agent. Thus, the scheme faces some of the constraints already present in other DNP strategies. For example, we do not consider the problem of (nuclear) spin diffusion from the polarizing agent. While an inefficient magnetization transport can degrade the performance of the procedure, a fair

assessment of spin diffusion across the barrier goes beyond the scope of this manuscript [26,27].

APPENDIX B: ESTIMATING RABI AMPLITUDES

We provide here an estimate of the transition-matrix element between the states $|0, -1/2\rangle$ and $|-1, +1/2\rangle$ (and analogously between $|0, +1/2\rangle$ and $|-1, -1/2\rangle$). First, we introduce the rf driving,

$$H_{\text{rf}} = -2\Omega_e \cos(\omega t) S_x \quad (\text{B1})$$

where $\Omega_e = \gamma_e B_1$ stands for the bare electronic Rabi amplitude. For simplicity, we are assuming the rf drives only the electronic transition $|0\rangle \leftrightarrow |-1\rangle$, but it is easy to show that the inclusion of a term in the form of $-2\Omega_n \cos(\omega t) I_x$, with $\Omega_n = \gamma_n B_1$, has no major impact.

We first write the matrix representation of the Hamiltonian, H , in Eq. (1) and the time-dependent H_{rf} in the ordered basis $\{|0, +1/2\rangle, |0, -1/2\rangle, |-1, +1/2\rangle, |-1, -1/2\rangle\}$:

$$H + H_{\text{rf}} = \begin{pmatrix} -\frac{\gamma_n B}{2} & 0 & -\Omega_e \cos(\omega t) & 0 \\ 0 & +\frac{\gamma_n B}{2} & 0 & -\Omega_e \cos(\omega t) \\ -\Omega_e \cos(\omega t) & 0 & -\frac{(\gamma_n B + A_{zz})}{2} + \delta_e & -\frac{A_{zx}}{2} \\ 0 & -\Omega_e \cos(\omega t) & -\frac{A_{zx}}{2} & \frac{\gamma_n B + A_{zz}}{2} + \delta_e \end{pmatrix}, \quad (\text{B2})$$

where we recall the energy detuning, $\delta_e = |\gamma_e|(B - B_c)$, as defined in Sec. II. Now, we change the nuclear-quantization axis to account for the hyperfine-induced hybridization. In this representation, the nuclear-quantization axis is defined by the vector

$$\vec{Z} = m_S A_{zx} \mathbf{i} + (m_S A_{zz} - \gamma_n B) \mathbf{k}, \quad (\text{B3})$$

forming an electron-spin-dependent angle with the z axis given by

$$\tan \theta_{m_S} = \frac{m_S A_{zx}}{(m_S A_{zz} - \gamma_n B)}. \quad (\text{B4})$$

On the other hand, the energy splitting is given by

$$\Delta_{m_S} = |\vec{Z}(m_S)| = \sqrt{(m_S A_{zx})^2 + (m_S A_{zz} - \gamma_n B)^2}. \quad (\text{B5})$$

This new matrix representation yields

$$[H + H_{\text{rf}}]_{\vec{Z}} = \begin{pmatrix} -\frac{\gamma_n B}{2} & 0 & -\Omega_e \cos(\omega t) c_1 & \Omega_e \cos(\omega t) s_1 \\ 0 & +\frac{\gamma_n B}{2} & -\Omega_e \cos(\omega t) s_1 & -\Omega_e \cos(\omega t) c_1 \\ -\Omega_e \cos(\omega t) c_1 & -\Omega_e \cos(\omega t) s_1 & -\frac{\Delta_{-1}}{2} + \delta_e & 0 \\ \Omega_e \cos(\omega t) s_1 & -\Omega_e \cos(\omega t) c_1 & 0 & \frac{\Delta_{-1}}{2} + \delta_e \end{pmatrix}, \quad (\text{B6})$$

where $c_1 = \cos(\theta_{-1}/2)$ and $s_1 = \sin(\theta_{-1}/2)$.

The Hamiltonian in Eq. (B6) already indicates the magnitude of the transition-matrix element between states $|0, -1/2\rangle$ and $|-1, +1/2\rangle$ (and between $|0, +1/2\rangle$ and $|-1, -1/2\rangle$). For example, in the case where $B = 1$ T, $A_{zz} = A_{zx} = 10$ MHz, and assuming $\Omega_e = 30$ MHz, we get an estimate of $\Omega_e s_1/2 \sim 3$ MHz (corresponding to submicrosecond inversion pulse durations). We refer the reader to Ref. [37] for a related discussion.

-
- [1] H. S. Leff and A. F. Rex, *Maxwell's demon: Entropy, information, computing* (Taylor & Francis Ltd, United Kingdom, 2002).
- [2] J. Klatzow, J. N. Becker, P. M. Ledingham, C. Weinzetl, K. T. Kaczmarek, D. J. Saunders, J. Nunn, I. A. Walmsley, R. Uzdin, and E. Poem, Experimental Demonstration of Quantum Effects in the Operation of Microscopic Heat Engines, *Phys. Rev. Lett.* **122**, 110601 (2019).
- [3] P. Hänggi, F. Marchesoni, and F. Nori, Brownian motors, *Ann. Phys.* **14**, 51 (2005).
- [4] E. M. Craig, N. J. Kuwada, B. J. Lopez, and H. Linke, Feedback control in flashing ratchets, *Ann. Phys.* **17**, 115 (2008).
- [5] K. Gopalsamy, *Stability and oscillations in delay differential equations of population dynamics* (Kluwer Academic Publishers, Dordrecht, The Netherlands, 1992).
- [6] D. F. Hendry, The encompassing implications of feedback versus feedforward mechanisms in econometrics, *Oxf. Econ. Pap.* **40**, 132 (1988).
- [7] S. R. Neves and R. Iyengar, Modeling of signaling networks, *BioEssays* **24**, 1110 (2002).
- [8] F. Bloch, Nuclear induction, *Phys. Rev.* **70**, 460 (1946).
- [9] M. A. McCoy and R. R. Ernst, Nuclear spin noise at room temperature, *Chem. Phys. Lett.* **159**, 587 (1989).
- [10] T. Sleator and E. L. Hahn, Nuclear-spin noise and spontaneous emission, *Phys. Rev. B* **36**, 1969 (1987).
- [11] K. Chandra, J. Schlagnitweit, C. Wohlschlagler, A. Jerschow, and N. Müller, Spin-noise-detected two-dimensional Fourier-transform NMR spectroscopy, *J. Phys. Chem. Lett.* **4**, 3853 (2013).
- [12] S. A. Crooker, D. G. Rickel, A. V. Balatsky, and D. L. Smith, Spectroscopy of spontaneous spin noise as a probe of spin dynamics and magnetic resonance, *Nature* **431**, 49 (2004).
- [13] N. Muller and A. Jerschow, Nuclear spin noise imaging, *Proc. Natl. Acad. Sci. U. S. A.* **103**, 6790 (2006).
- [14] C. A. Meriles, J. Liang, G. Goldstein, P. Cappellaro, J. Hodges, J. Maze, and M. D. Lukin, Imaging mesoscopic nuclear spin noise with a diamond magnetometer, *J. Chem. Phys.* **133**, 124105 (2010).
- [15] A. Laraoui, F. Dolde, C. Burk, F. Reinhard, J. Wrachtrup, and C. A. Meriles, High-resolution correlation spectroscopy of ^{13}C spins near a nitrogen-vacancy center in diamond, *Nat. Commun.* **4**, 1651 (2013).
- [16] R. Budakian, H. J. Mamin, B. W. Chui, and D. Rugar, Creating order from random fluctuations in small spin ensembles, *Science* **307**, 408 (2005).
- [17] C. L. Degen, M. Poggio, H. J. Mamin, and D. Rugar, Role of Spin Noise in the Detection of Nanoscale Ensembles of Nuclear Spins, *Phys. Rev. Lett.* **99**, 250601 (2007).
- [18] P. Peddibhotla, F. Xue, H. I. T. Hauge, S. Assali, E. P. A. M. Bakkers, and M. Poggio, Harnessing nuclear spin polarization fluctuations in a semiconductor nanowire, *Nat. Phys.* **9**, 631 (2013).
- [19] B. Plainchont, P. Berruyer, J.-N. Dumez, S. Jannin, and P. Giraudeau, Dynamic nuclear polarization opens new perspectives for NMR spectroscopy in analytical chemistry, *Anal. Chem.* **90**, 3639 (2018).
- [20] J. H. Ardenkjaer-Larsen, On the present and future of dissolution-DNP, *J. Magn. Reson.* **264**, 3 (2016).
- [21] A. S. L. Thankamony, J. J. Wittmann, M. Kaushik, and B. Corzilius, Dynamic nuclear polarization for sensitivity enhancement in modern solid-state NMR, *Prog. Nucl. Magn. Reson. Spectrosc.* **102**, 120 (2017).
- [22] D. Pagliero, K. R. Koteswara Rao, P. R. Zangara, S. Dhomkar, H. H. Wong, A. Abril, N. Aslam, A. Parker, J. King, C. E. Avalos, *et al.*, Multispin-assisted optical pumping of bulk ^{13}C nuclear spin polarization in diamond, *Phys. Rev. B* **97**, 024422 (2018).
- [23] R. Wunderlich, J. Kohlrutz, B. Abel, J. Haase, and J. Meijer, Optically induced cross relaxation via nitrogen-related defects for bulk diamond ^{13}C hyperpolarization, *Phys. Rev. B* **96**, 220407(R) (2017).
- [24] D. A. Broadway, J.-P. Tetienne, A. Stacey, J. D. A. Wood, D. A. Simpson, L. T. Hall, and L. C. L. Hollenberg, Quantum probe hyperpolarisation of molecular nuclear spins, *Nat. Commun.* **9**, 1246 (2018).
- [25] D. Pagliero, P. R. Zangara, J. Henshaw, A. Ajoy, R. H. Acosta, N. Manson, J. Reimer, A. Pines, and C. A. Meriles, Magnetic-field-induced delocalization in hybrid electron-nuclear spin ensembles, *Phys. Rev. B* **103**, 064310 (2021).
- [26] D. Pagliero, P. Zangara, J. Henshaw, A. Ajoy, R. H. Acosta, J. A. Reimer, A. Pines, and C. A. Meriles, Optically pumped spin polarization as a probe of many-body thermalization, *Sci. Adv.* **6**, eaaz6986 (2020).
- [27] Q. Stern, S. F. Cousin, F. Mentink-Vigier, A. C. Pinon, S. J. Elliott, O. Cala, and S. Jannin, Direct observation of hyperpolarization breaking through the spin diffusion barrier, *Sci. Adv.* **7**, eabf5735 (2021).
- [28] J. Henshaw, D. Pagliero, P. R. Zangara, B. Franzoni, A. Ajoy, R. Acosta, J. A. Reimer, A. Pines, and C. A. Meriles, ^{13}C dynamic nuclear polarization in diamond via a microwave-free 'integrated' cross effect, *Proc. Natl. Acad. Sci. U. S. A.* **116**, 18334 (2019).
- [29] T. V. Can, R. T. Weber, J. J. Walsh, T. M. Swager, and R. G. Griffin, Frequency-swept integrated solid effect, *Angew. Chem., Int. Ed. Engl.* **56**, 6744 (2017).
- [30] C. A. Meriles and P. R. Zangara, Microwave-Free Dynamic Nuclear Polarization via Sudden Thermal Jumps, *Phys. Rev. Lett.* **128**, 037401 (2022).
- [31] T. Maly, G. T. Debelouchina, V. S. Bajaj, K.-N. Hu, C.-G. Joo, M. L. Mak-Jurkauskas, J. R. Sirigiri, P. C. A. van der Wel, J. Herzfeld, R. J. Temkin, and R. G. Griffin, Dynamic nuclear polarization at high magnetic fields, *J. Chem. Phys.* **128**, 052211 (2008).
- [32] K. Binnemans, Interpretation of europium(III) spectra, *Coord. Chem. Rev.* **295**, 1 (2015).

- [33] D. Su, K. Wu, R. Saha, C. Peng, and J.-P. Wang, Advances in magnetoresistive biosensors, *Micromachines* **11**, 34 (2020).
- [34] I. Giouroudi and E. Hristoforou, Perspective: Magnetoresistive sensors for biomedicine, *J. Appl. Phys.* **124**, 030902 (2018).
- [35] H. Toida, Y. Matsuzaki, K. Kakuyanagi, X. Zhu, W. J. Munro, H. Yamaguchi, and S. Saito, Electron paramagnetic resonance spectroscopy using a single artificial atom, *Commun. Phys.* **2**, 33 (2019).
- [36] D. Vasyukov, Y. Anahory, L. Embon, D. Halberthal, J. Cuppens, L. Neeman, A. Finkler, Y. Segev, Y. Myasoedov, M. L. Rappaport, *et al.*, A scanning superconducting quantum interference device with single electron spin sensitivity, *Nat. Nanotech.* **8**, 639 (2013).
- [37] P. R. Zangara, D. Pagliero, A. Ajoy, R. H. Acosta, J. A. Reimer, and C. A. Meriles, Nuclear spin temperature reversal via continuous radio-frequency driving, *Phys. Rev. B* **103**, 085205 (2021).